PCCP

PAPER

View Article Online
View Journal | View Issue

Cite this: *Phys. Chem. Chem. Phys.*, 2019, **21**, 13758

$LiAl_5O_8$ as a potential coating material in lithium-ion batteries: a first principles study†

Sijia Mo, Bingkai Zhang, Kecheng Zhang, Shunning Li* and Feng Pan *

Received 10th May 2019,
Accepted 30th May 2019

DOI: 10.1039/c9cp02650a

rsc.li/pccp

Coating materials in lithium-ion batteries (LIBs) have attracted extensive attention due to their ability to retard the decay of electrochemical performance in long-term cycling. Most of these coating materials, however, exhibit inferior ionic diffusivity. Herein, we report a novel coating material, $LiAl_5O_8$, which possesses a spinel-type structure. Our first principles calculation results show that the diffusion coefficient of Li ions in $LiAl_5O_8$ is over thirty orders of magnitude higher than that of Al_2O_3, and its electrochemical stability window is sufficiently wide, from 0.80 to 4.08 V *versus* Li/Li^+. The facile Li ion diffusion pathways and high electrochemical stability make $LiAl_5O_8$ an effective coating material for next-generation LIBs.

1. Introduction

Research into coating materials for electrodes in lithium-ion batteries (LIBs) has emerged as an important area of focus due to their essential role in improving the cyclic performance and enabling high-voltage operation of the batteries.[1,2] Nowadays, a major concern about the $LiPF_6$-based electrolytes, commonly used in the market for LIBs, is their reactivity with electrodes that generally results in the consumption of the electrolytes and the dissolution of redox-active elements in the electrodes. The coating materials can serve as a physical protective barrier lying between the electrode and electrolyte, thus suppressing the oxidation of electrolyte compounds and the corrosion of charged electrodes. Most of the promising coating materials are in the binary metal oxide system, including Al_2O_3, ZnO, MgO, TiO_2, ZrO_2, *etc.*[3–6] However, these materials exhibit comparatively poor ionic transport properties, with migration barriers of over 0.9 eV for Li ion diffusion,[7] which probably resulted from the narrow diffusion pathways in the crystalline structures of these oxides. Such low ionic conductivity necessitates the fabrication of extremely thin coating layers (below 1 nm)[8] or the use of their counterparts in the amorphous form.[9,10] Given that a higher lithium content in a solid state electrolyte (SSE) has the potential to modify the ionic conductivity by eliminating the energy difference for lithium located at different sites along the diffusion paths,[11] we can expect that this principle is transferable to the coating materials listed above. Under this consideration, some researchers have turned their attention to the exploration of prelithiated oxides, such as $LiAlO_2$, Li_2ZrO_3, *etc.*,[12–15] in the last few years. Materials of this type have offered new opportunities for the development of next-generation coating materials for LIBs, but the family of these oxides is still small. Here we propose a novel material, $LiAl_5O_8$, which shows superior ionic conductivity as compared with Al_2O_3 and holds promise in the application of coating materials for electrodes in LIBs.

$LiAl_5O_8$ was previously used as a phosphor with interesting optical properties[16] and has recently been detected in an alumina coating layer between the lithium metal anode and a garnet-type solid-state electrolyte after lithiation.[17] At room temperature, bulk $LiAl_5O_8$ crystallizes in an inverse spinel structure, characterized by the $P4_332$ space group.[18] The spinel framework can potentially permit a high ionic conductivity with a three-dimensional (3D) percolating diffusion network, as demonstrated in some famous cathode materials like $LiMn_2O_4$.[19,20] Therefore, it is anticipated that bulk $LiAl_5O_8$ can have high Li-ion mobility. Nevertheless, to the best of our knowledge, no experiment has been reported on the utilization of this material as a coating layer except a computation research by a high-throughput method,[21] but the mechanism for Li diffusion has been unknown so far. In this work, we apply first principles density functional theory (DFT) to understand the electrochemical characteristics of $LiAl_5O_8$ and the mechanism of ionic transport in it. We calculate the defect formation energies of Li vacancies and interstitials at 0 V and 4 V *versus* Li/Li^+, respectively, which show that Li interstitial is the dominant diffusion carrier at low electrode potential while Li vacancies are the main carrier type at high electrode potential. We employ nudged elastic band (NEB) simulations to investigate the Li transport mechanism and find that the mobility of Li in $LiAl_5O_8$ is substantially higher than that in Al_2O_3 and MgO. In addition,

School of Advanced Materials, Peking University, Shenzhen Graduate School, Shenzhen 518055, People's Republic of China. E-mail: lisn@pkusz.edu.cn, panfeng@pkusz.edu.cn

† Electronic supplementary information (ESI) available. CCDC 1595312. For ESI and crystallographic data in CIF or other electronic format see DOI: 10.1039/c9cp02650a

we predict a wide electrochemical window for $LiAl_5O_8$, guaranteeing that this coating material is electrochemically stable under operation.

2. Methods

All calculations in this research were performed by the implementation of plane wave DFT in the Vienna *ab initio* simulation package (VASP)[22] with projector augmented wave (PAW) potentials.[23] The exchange–correlation part of the density functional was treated within the generalized gradient approximation (GGA) of Perdew–Burke–Ernzerhof (PBE).[24] Valence electron configurations for elemental constituents are as follows: Li-$2s^1$, Al-$3s^2 3p^1$ and O-$2s^2 2p^4$. The cut-off energy chosen for the plane-wave expansion was set to 500 eV. Monkhorst–Pack[25] k-point meshes ($2 \times 2 \times 2$) were used to sample the Brillouin zones. Convergence was assumed when the total energy difference was below 1.0×10^{-6} eV per atom and the residual forces were below 0.01 eV $Å^{-1}$. A denser k-point mesh of $8 \times 8 \times 8$ has been used to calculate the density of states (DOS) in GGA methods.

The point defect properties were calculated using a $2 \times 1 \times 1$ supercell. The formation energy of a defect for a charge state q is given as a function of Fermi energy:[26]

$$E_f = E_{def} - E_{bulk} - n\mu_{Li} + q(\varepsilon_F + E_V) \quad (1)$$

where E_{def} and E_{bulk} represent the total energies of the defected and the pristine $LiAl_5O_8$ supercells, respectively. The number of Li^+ added to ($n > 0$) or removed from ($n < 0$) the pristine supercell is n when defects are generated. In the charge state, an additional homogeneous neutralizing background charge is applied by VASP to maintain charge neutrality of the system and guarantee the energy convergence. ε_F is the Fermi energy and E_V is the energy of the valence band maximum for the pristine $LiAl_5O_8$ unit cell. μ_{Li} represents the chemical potential of lithium. In accord with a previous study,[27,28] μ_{Li} is related to the electrode potential ϕ *versus* Li/Li^+ as

$$\mu_{Li}(\phi) = \mu^0_{Li} - e\phi \quad (2)$$

where μ^0_{Li} is the chemical potential of bulk Li metal, which is set to −1.89 eV taken from the energy of one Li atom in bulk Li metal from DFT calculation; and e is the elementary charge.

To search for the possible Li-ion migration pathways and the corresponding migration barriers, the climbing image nudged elastic band (CI-NEB) method was used.[29] A chain of five initial images between two local energy minima structures was first set by linear interpolation and then fully relaxed.

We estimate the diffusion coefficient *via* the following fomula[30]

$$D = \frac{1}{2}\nu(\Delta x)^2 e^{[-E_m/k_B T]} \quad (3)$$

where Δx is the hop distance, ν is the lattice vibrational frequency with a typical value of 10^{13} Hz[31–33] and E_m is the migration barrier. k_B is the Boltzmann constant and T is the temperature which we set to 300 K in this work.

The grand potential phase diagram[34] was established to investigate the electrochemical stability of $LiAl_5O_8$. The grand potential phase diagram was generated using the Python Materials Genomics (pymatgen) library[35] which is an open source materials library. The code package of Deng *et al.*[36] was used to accelerate the calculation process.

3. Results and discussion

3.1. Perfect $LiAl_5O_8$ crystal

$LiAl_5O_8$ can be described as $(Al)_{tet}(Li_{1/2}Al_{3/2})_{oct}O_4$, which is composed of corner-linked Al–O tetrahedra and edge-shared Li/Al–O octahedra, as shown in Fig. 1. All of the Li ions are distributed in octahedral sites, whereas two fifths of Al ions are at the tetrahedral sites and others at octahedral sites. Each Li–O octahedron is surrounded by 6 Al–O octahedra, with another 6 Al–O tetrahedra as the second nearest neighbors. All the four Li ions in the unit cell are identical to each other, owing to the high symmetry of the compound, which means that each Li ion has the same environment and therefore the same diffusion path.

Table 1 lists the calculation results of lattice parameters for $LiAl_5O_8$ in comparison with the data obtained with GGA from Materials Project (MP)[37] and the experimental data obtained by Kriens *et al.* at room temperature.[38] The lattice constant of $LiAl_5O_8$ in this study is 7.972 Å, consistent with the experimental data (within 1% error). GGA was used to provide a rigorous result for the density of states (DOS) of $LiAl_5O_8$, as shown in Fig. 2. A band gap as large as 5.34 eV indicates that $LiAl_5O_8$ is a good electron insulator, which is potent in blocking the electron leakage and protecting against electrode corrosion.[39]

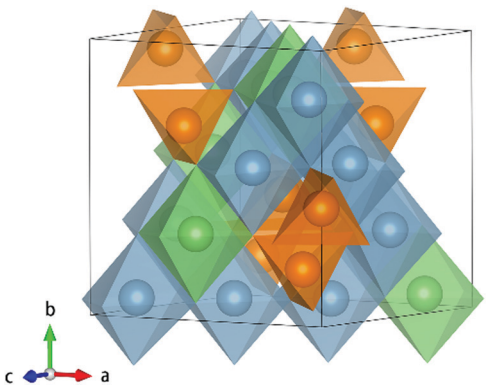

Fig. 1 Structure of $LiAl_5O_8$. AlO_4 tetrahedra, LiO_6 octahedra and AlO_6 octahedra are shown in orange, green and blue, respectively.

Table 1 Calculated results of lattice parameters, atomic positions for $LiAl_5O_8$ as compared with previous theoretical and experimental data

		Cal. (this work)	Cal. (MP)	Exp. (ref. 38)
a (Å)		7.972	7.987	7.903
Atom	Site	(x, y, z)	(x, y, z)	
Li	4b	(0.125, 0.875, 0.375)	(0.125, 0.875, 0.375)	
Al	8d	(0.368, 0.882, 0.125)	(0.369, 0.881, 0.125)	
Al	4a	(0.003, 0.497, 0.503)	(0.002, 0.498, 0.502)	
O	8d	(0.365, 0.382, 0.866)	(0.365, 0.383, 0.864)	

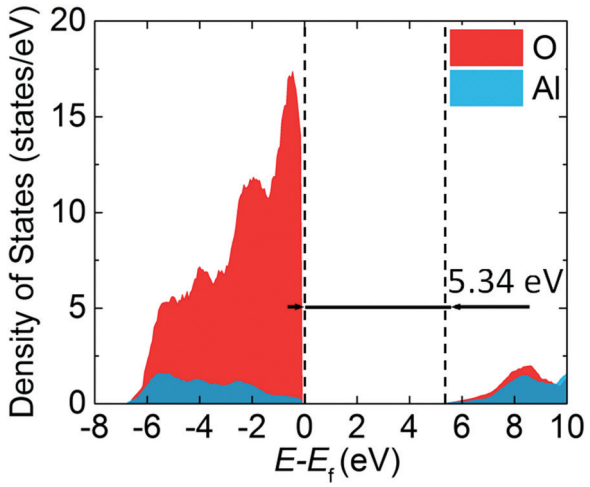

Fig. 2 Density of states of $LiAl_5O_8$. Energies are referenced to the Fermi level.

3.2. Defects in $LiAl_5O_8$

As the valence state of Al ions is hard to change, $LiAl_5O_8$ can hardly exhibit off-stoichiometric composition during battery operation. It implies that the ionic conductivity of the $LiAl_5O_8$ coating material should be dictated by the intrinsic point defects such as Li vacancies and interstitials. Following eqn (1), we first calculated the formation energies of the point defects V_{Li}^0 and Li_i^0 in the neutral state. Electrode potential ϕ was discussed in two situations in this study. We considered two possible cases where $LiAl_5O_8$ is used as a coating material for cathode and anode electrodes, respectively. When $LiAl_5O_8$ is used as an anode electrode coating material, such as lithium metal, ϕ is set to 0 V *versus* Li/Li^+; in the cathode case, the potential ϕ is set to 4 V. μ_{Li} at different voltages will vary greatly, affecting the value of the defect formation energy. Table 2 lists the positions and the defect formation energies with electrode potentials of 0 V and 4 V, as well as the atomic configurations in the vicinity of the defects.

Since four Li ions in the unit cell are identical to each other, there is only one configuration for Li vacancies. Unlike Li vacancies, there are three crystallographically inequivalent sites for Li interstitials. Configuration I (Int-I), in which the Li interstitial is located in the tetrahedral interstice (I_{tet}) of the O sublattice, corresponds to the lowest formation energy at ϕ = 0 V. The Li interstitial pushes away the nearest Li at the lattice site by around 0.55 Å, which mainly stems from the short distance (2.01 Å) between the interstitial and the Li nearby. The displacement of lattice atoms imposed by the Li interstitial is much smaller for configuration Int-II, where excess Li is located in the octahedral interstice (I_{oct}), having the largest free volume among all the configurations. However, it has a relatively high formation energy, 0.32 eV, above that of Int-I. This runs somewhat counter to the intuition that the larger the open space and the coordination number to the lattice O, the lower the defect formation energy will be. The reason lies in that Li at this interstitial site is at the midpoint of two Al with a Li–Al distance of 2.07 Å. The large electrostatic repulsion of Al ions to the Li interstitial would raise the energy of the system, making this site unfavorable for Li occupation. Even more distinctive is configuration Int-III, which is calculated to be 1.16 eV higher in formation energy than that of Int-I. In this configuration, the Li interstitial is in a tetrahedral interstice (different from Int-I) and the LiO_4 tetrahedron is face-shared with three Al–O polyhedra, thus yielding large energy penalty in the system.

Table 2 The positions of defects, the atomic configurations in the vicinity of the defects, and the corresponding defect formation energies at different ϕ

Label	Position	Atomic configuration	E_f (ϕ = 0 V) (eV)	E_f (ϕ = 4 V) (eV)
Vacancy	(0.13, 0.88, 0.38)		5.09	1.09
Int-I	(0.21, 0.78, 0.50)		3.55	7.55
Int-II	(0.37, 0.87, 0.62)		3.87	7.87
Int-III	(0.25, 0.48, 0.48)	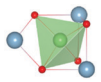	4.71	8.71

It is found that the formation energy of Li vacancies is much higher than Li interstitial at 0 V (corresponding to the lithium metal anode environment), which is calculated to be 5.09 eV. And the formation energy of the three Li interstitials is 3.55 eV, 3.87 eV and 4.71 eV, respectively. This translates into a concentration over 25 orders of magnitude higher than that of Li vacancies according to $c = N\exp(-E_f/kT)$, which implies that Li interstitials are dominant under anodic conditions. However, the situation is changed at an electrode potential of 4 V (corresponding to the high-voltage cathode environment). The formation energy of Li vacancies is 1.09 eV, apparently lower than that of Li interstitials, *i.e.* 7.55 eV, 7.87 eV and 8.71 eV, respectively, indicating that under cathodic conditions, the concentration of Li vacancies is much larger.

Fig. 3 shows the formation energies of Li vacancies and interstitials at different charge states as a function of the Fermi level at 0 V. The formation energies of excess electrons and holes in $LiAl_5O_8$ are also given as comparison. It can be seen that the formation energies of Li_i^+ and V_{Li}^- are always lower than those of Li_i^0 and V_{Li}^0, implying that Li would spontaneously ionize in $LiAl_5O_8$, similar to the cases of other coating materials.[7] This can be rationalized by the fact that Li_i^0 and V_{Li}^0 will change the valence states of Al and O, which are substantially unstable. Therefore, charged defects (Li ion vacancies and Li ion interstitials) should be expected as the charge carriers in $LiAl_5O_8$ and will be employed for the calculation of migration barriers in the following discussion. Moreover, the Fermi level will be pinned at 3.6 eV above the VBM so that the concentration of positive and negative charge species (Li_i^+ and V_{Li}^-, respectively) is equal, that is, charge neutrality is kept in the system. We may expect that the ionic diffusivity can dictate the ionic conductivity when comparing these two kinds of charge carriers.

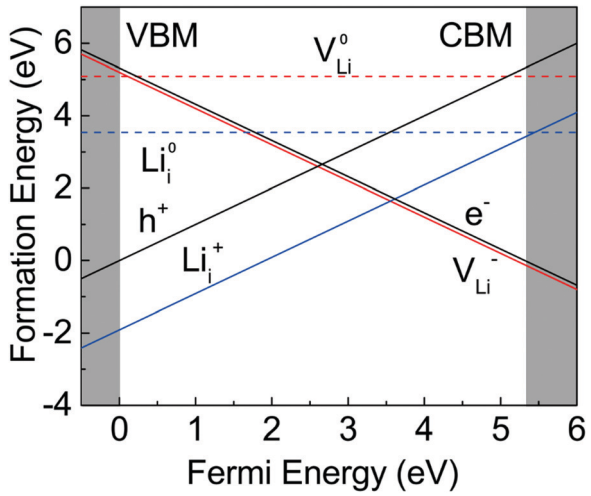

Fig. 3 Formation energies for Li vacancies and interstitials at different charge states when the electrode potential is 0 V, as well as that for excess electrons and holes.

3.3. Ionic transport in $LiAl_5O_8$

The ionic conductivity of $LiAl_5O_8$ stems from the diffusion of ionic point defects, including Li_i^+ and V_{Li}^-. The migration of V_{Li}^- is equivalent to the migration of one of its nearest Li neighbors to the vacant site. After careful examination of the structure of $LiAl_5O_8$, we find that there is only one diffusion path for V_{Li}^-, as shown in Fig. 4a and b. Along this path, the migrating Li will pass through the I_{oct} site (corresponding to Int-II), and then the vacant site, rather than along the straight line from the first vacant site to the next. This is due to the fact that at the midpoint of the straight line there is an adjacent lattice Al. The distance between the migrating Li and the lattice Al is below 2 Å, resulting in a large electrostatic repulsion. It should be mentioned that the above images differ from configurations Int-I and Int-II by that two Li ion vacancies at the lattice sites are now in the vicinity of the Li ion interstitial. The vacancy migration barrier is calculated to be as high as 2.86 eV in Fig. 4c, which is to be expected since a Li ion vacancy and a Li ion interstitial will be generated simultaneously when the migrating Li leaves the lattice site.

Next, we investigate the diffusion of Li_i^+ in $LiAl_5O_8$. Since the formation energy of Int-III is much higher than those of Int-I and Int-II, it is expected that Li will not pass this site during diffusion. As for Int-II, the net distance for each diffusion step is 2.88 Å, higher than that for Int-I with a value of 2.10 Å. Considering further that Int-I possesses lower formation energy than Int-II, we select Int-I as the end point when searching the diffusion pathways of Li_i^+ in $LiAl_5O_8$. Two kinds of diffusion events are involved, both of which are indispensable for a 3D percolating diffusion network: a diffusion path (A → B) passing through the octahedral interstice and another path (B → C) surrounding a Li lattice site, as illustrated in Fig. 5a and b. The first path describes the $I_{tet} \rightarrow I_{oct} \rightarrow I_{tet}$ hopping. The calculated diffusion barrier is 0.33 eV, which is substantially lower than that of Li ion vacancy diffusion, as no additional vacancy or interstitial site is generated in this path. The saddle point corresponds to a configuration in which the Li crosses near the center of an O-triangle, *i.e.* the face shared between the Li_iO_4 tetrahedron and Li_iO_6 octahedron. This diffusion path is connected by the second kind of pathway where the Li at an I_{tet} site migrates to another one nearby, both surrounding the same Li lattice site. Two mechanisms may be responsible for this path, the direct-hopping mechanism and knock-off mechanism.[40] In the direct-hopping mechanism, the Li ion interstitial passes through the shared edge between two Li_iO_4 tetrahedra, leading to relatively shorter Li–O bonds (1.37 Å) than those when Li is located in the center of an O-triangle (2.11 Å). In the knock-off mechanism, on the other hand, the Li ion interstitial will push the neighboring Li at the lattice site into the target interstitial site while the lattice site is filled with the original Li ion interstitial. The knock-off mechanism yields longer Li–O bonds along the path as compared with the direct-hopping mechanism, yet we find a lower diffusion barrier for the latter one (0.11 eV). This may be rationalized by the brief appearance of a Li ion vacancy during the concerted migration of the two Li ions in the knock-off mechanism.

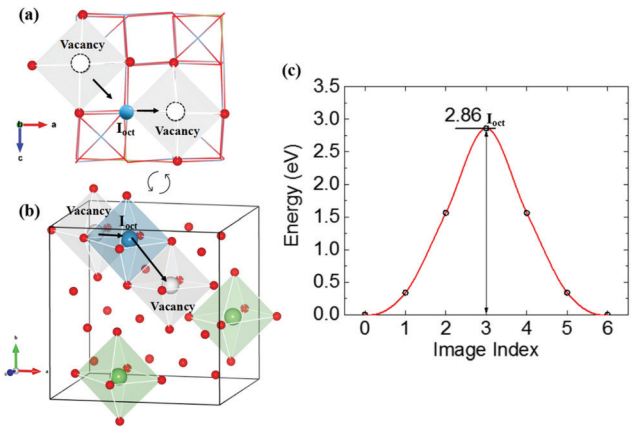

Fig. 4 Diffusion pathway of V_{Li}^- in (a) sectional view and (b) stereo view, and the corresponding (c) activation barrier.

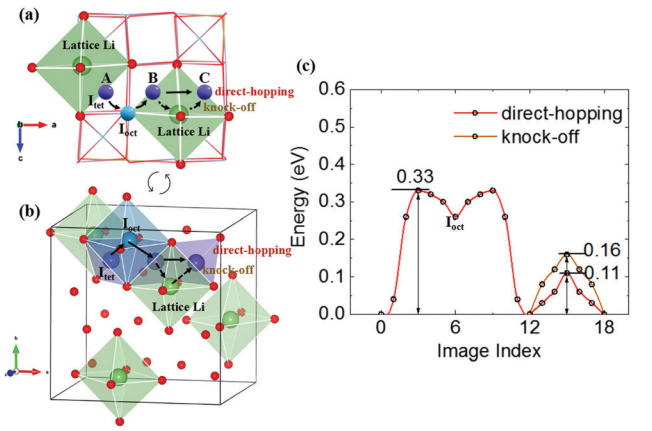

Fig. 5 Diffusion pathways of Li_i^+ in (a) sectional view and (b) stereo view, and the corresponding (c) activation barriers.

As the energy barrier for Li_i^+ is much lower than that of V_{Li}^-, we could make the conclusion that the ionic conductivity in $LiAl_5O_8$ is mainly contributed by Li ion interstitials. The overall diffusion barrier for the Li ion interstitial in $LiAl_5O_8$ is 0.33 eV and from eqn (3) the diffusion coefficient is 3.6×10^{-8} cm^2 s^{-1}. For comparison, we calculate the energy barrier of Li_i^+ diffusion in Al_2O_3 and MgO in the same computational scheme, as shown in Fig. 6. The barriers are extremely high (2.69 eV for Al_2O_3 and 2.18 for MgO) and the corresponding diffusion coefficient is 9.3×10^{-48} cm^2 s^{-1} and 3.3×10^{-39} cm^2 s^{-1}, respectively. The diffusion coefficient of Li ions in $LiAl_5O_8$ is over thirty orders of magnitude higher than that of Al_2O_3, implying a better performance of the battery when replacing Al_2O_3 coating with $LiAl_5O_8$. We also compare the migration barrier and diffusion coefficient to those of amorphous Al_2O_3[9] and those of other typical compounds in the solid electrolyte interphase (SEI) such as Li_2CO_3, LiF and Li_2O in the literature.[41–43] Obviously, the ionic conductivity of $LiAl_5O_8$ is superior to most of these materials except Li_2CO_3 as tabulated in Table 3, which demonstrates the advantageous nature of this coating material.

3.4. Electrochemical stability

Similar to the electrolyte in a battery, the coating layer should have acceptable electrochemical stability so that the highest voltage output of the battery can be achieved. The limited stability of the coating material would result in the decomposition of the compound, either leaving the electrode unprotected or forming undesired products at the interfaces that exhibit low permeability to Li ions. In addition, the coating materials with a broad electrochemical window can function as a passivation layer to suppress the decomposition of electrolyte, especially in the battery system with a high-voltage cathode and a low-voltage anode.[44] Furthermore, most solid-state electrolyte materials have been demonstrated to

Table 3 Migration barriers and diffusion coefficients at 300 K of $LiAl_5O_8$, other metal oxide coating materials and typical compounds in SEI

Material	Migration barrier (eV)	Diffusivity (cm^2 s^{-1})
$LiAl_5O_8$	0.33	3.6×10^{-8}
Al_2O_3	2.69	9.3×10^{-48}
MgO	2.18	3.6×10^{-39}
am-Al_2O_3 (ref. 9)	0.73	5.9×10^{-17}
Li_2CO_3 (ref. 41)	0.24	1.2×10^{-6}
LiF (ref. 42)	0.73	7.1×10^{-15}
Li_2O (ref. 43)	0.47	1.6×10^{-10}

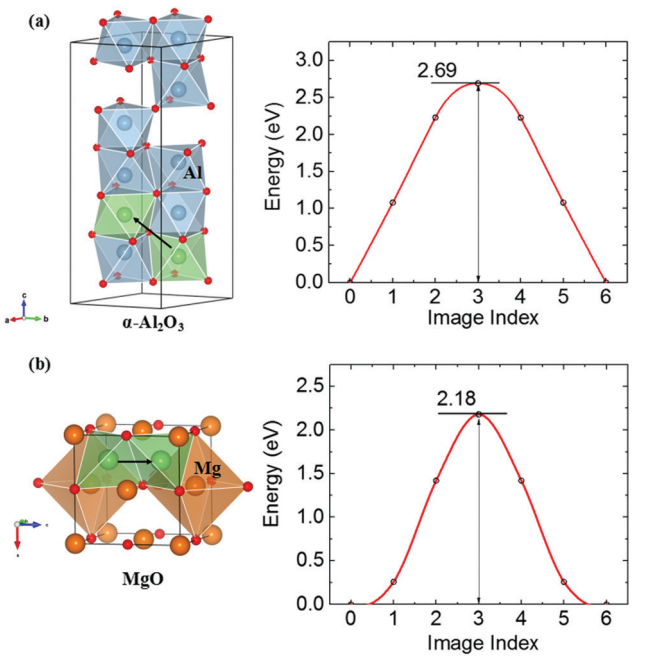

Fig. 6 Diffusion pathways and energy barrier of Li_i^+ in (a) Al_2O_3 and (b) MgO.

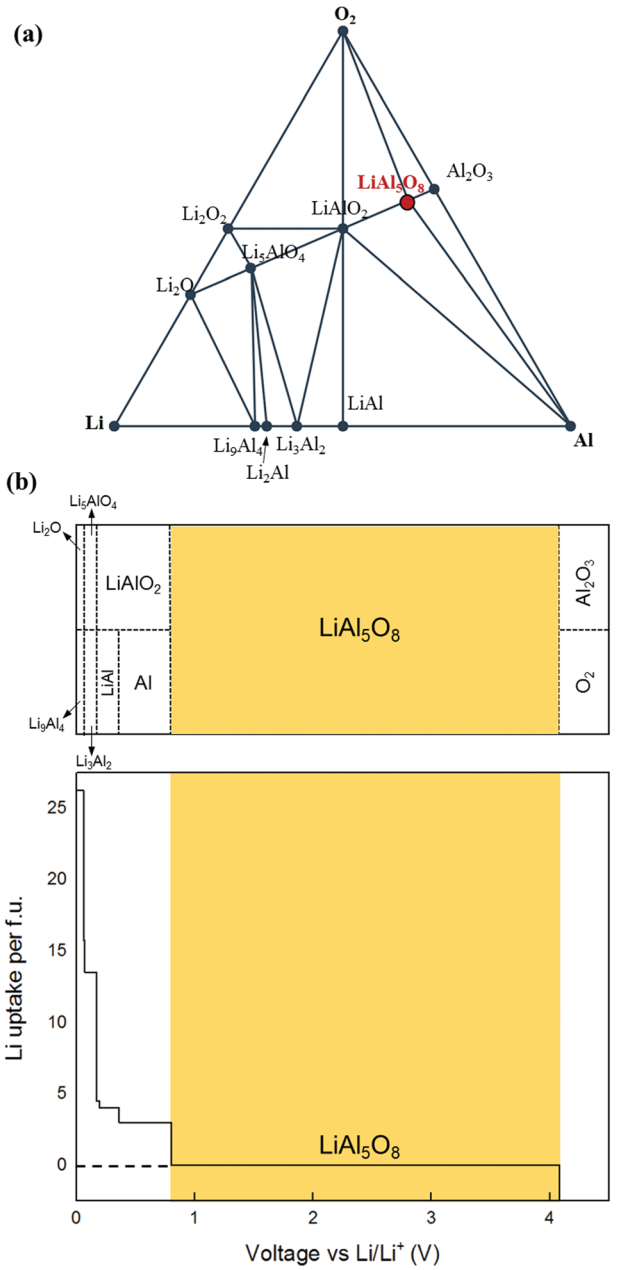

Fig. 7 (a) Li–Al–O ternary phase diagram. $LiAl_5O_8$ is marked in red font. (b) Equilibrium phase of $LiAl_5O_8$ at different potentials.

have narrow intrinsic electrochemical windows, and therefore suitable electrode coating materials can further broaden their electrochemical window so as to improve battery cycling performance.[45] Based on this consideration, a number of novel coating materials with wide electrochemical windows as the screening conditions have recently been developed.[46] A wide electrochemical window is another key indicator for $LiAl_5O_8$ in electrode coating.

Here, we examine the intrinsic thermodynamic electrochemical stability window of $LiAl_5O_8$. The Li–Al–O ternary phase diagram which determines the phase equilibria of $LiAl_5O_8$ at different Li chemical potentials is constructed by pymatgen, as shown in Fig. 7a. Higher Li chemical potential, *i.e.* lower electrode potential ϕ *versus* Li/Li^+ (according to eqn (2)), would correspond to compositions farther away from the Li end point in the phase diagram, and *vice versa*.

Our calculation demonstrates that the intrinsic stability window is relatively wide, from 0.80 to 4.08 V *versus* Li/Li^+. The phase equilibria at different potentials are identified according to the most thermodynamically favorable reaction products at given potentials, as shown in Fig. 7b. The reduction of $LiAl_5O_8$ starts at 0.80 V, where some of the Al atoms are reduced and form alloys with Li. A further decrease of the potential (0 V *versus* Li/Li^+) will promote the Li–Al alloying process until all the reduction products turn into Li_9Al_4 and Li_2O. On the other hand, the oxidization of $LiAl_5O_8$ takes place at 4.08 V, where the coating material transforms into Al_2O_3. Since Al_2O_3 can also be used as a coating layer, we may expect that even at voltage higher than 4.08 V, the coating layer can still offer effective protection to the electrode, although the rate capability will unavoidably be hampered.

We compare the electrochemical stability windows between $LiAl_5O_8$ and other prelithiated coating materials, as well as typical SSE materials. It is found that the electrochemical stability of $LiAl_5O_8$ can outperform other coating materials, as shown in Fig. 8. It is worth mentioning that $LiAl_5O_8$ has the highest oxidation voltage among other prelithiated coating materials, indicating that although $LiAl_5O_8$ has a lower migration energy barrier in a low voltage environment, it still holds promise for use in high voltage cathode coating application due to the excellent upper limit of the electrochemical window. As compared with SSEs, the electrochemical stability of $LiAl_5O_8$ is much more superior. Therefore, we can anticipate that $LiAl_5O_8$, with its high ionic conductivity, will profoundly improve the overall electrochemical performance of solid state batteries.

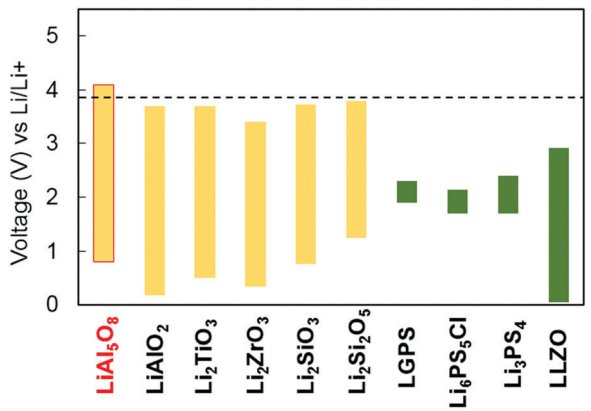

Fig. 8 Electrochemical stability window of $LiAl_5O_8$ (red frame rectangle), other prelithiated coating materials (yellow rectangle), and typical solid state electrolytes (green rectangle). The dashed line at 3.9 V corresponds to the equilibrium voltage of $LiCoO_2$.

4. Conclusions

In summary, we use DFT calculations to investigate the electrochemical properties of $LiAl_5O_8$ as a novel coating material for LIBs. It is shown that $LiAl_5O_8$ is a good electronic insulator with a large band gap of 5.34 eV. The Li ion interstitials have the migration barrier as low as 0.33 eV and possess high diffusivity in a 3D percolating network. The calculated diffusion coefficient is over thirty orders of magnitude higher than that of Al_2O_3 and MgO and well above those of other SEI compounds. The electrochemical stability window of $LiAl_5O_8$ is found to be 0.80–4.08 V, which can effectively broaden the electrochemical stability window of potential SSE materials. Overall, $LiAl_5O_8$ is a potential candidate for coating materials that can outperform its counterparts and therefore deserves further experimental examination.

Conflicts of interest

There are no conflicts to declare.

Acknowledgements

National Key R&D Program of China (2016YFB0700600), Shenzhen Science and Technology Research Grant (ZDSYS201707281026184), and Guangdong Key-lab Project (No. 2017B0303010130).

References

1 C. Li, H. P. Zhang, L. J. Fu, H. Liu, Y. P. Wu, E. Ram, R. Holze and H. Q. Wu, Cathode Materials Modified by Surface Coating for Lithium Ion Batteries, *Electrochim. Acta*, 2006, **51**, 3872–3883.

2 L. J. Fu, H. Liu, C. Li, Y. P. Wu, E. Rahm, R. Holze and H. Q. Wu, Surface Modifications of Electrode Materials for Lithium Ion Batteries, *Solid State Sci.*, 2006, **8**, 113–128.

3 A. M. Kannan, L. Rabenberg and A. Manthiram, High Capacity Surface-Modified $LiCoO_2$ Cathodes for Lithium-Ion Batteries, *Electrochem. Solid-State Lett.*, 2003, **6**, A16–A18.

4 Y. M. Lin, H. C. Wu, Y. C. Yen, Z. Z. Guo, M. H. Yang, H. M. Chen, H. S. Sheu and N. L. Wu, Enhanced High-Rate Cycling Stability of $LiMn_2O_4$ Cathode by ZrO_2 Coating for Li-Ion Battery, *J. Electrochem. Soc.*, 2005, **152**, A1526–A1532.

5 J. H. Wang, T. Fang and J. G. Duh, $LiCoO_2$ Cathode Material Coated with Nano-Crystallized ZnO by Sol-Gel Method, *Key Eng. Mater.*, 2005, **280–283**, 665–670.

6 J. H. Shim, S. Lee and S. S. Park, Effects of MgO Coating on the Structural and Electrochemical Characteristics of

$LiCoO_2$ as Cathode Materials for Lithium Ion Battery, *Chem. Mater.*, 2014, **26**, 2537–2543.

7 S. Z. Xu, R. M. Jacobs, H. M. Nguyen, S. Q. Hao, M. Mahanthappa, C. Wolverton and D. Morgan, Lithium Transport through Lithium-Ion Battery Cathode Coatings, *J. Mater. Chem. A*, 2015, **3**, 17248–17272.

8 Y. S. Jung, A. S. Cavanagh, A. C. Dillon, M. D. Groner, S. M. George and S. H. Lee, Enhanced Stability of $LiCoO_2$ Cathodes in Lithium-Ion Batteries Using Surface Modification by Atomic Layer Deposition, *J. Electrochem. Soc.*, 2010, **157**, A75–A81.

9 S. Q. Hao and C. Wolverton, Lithium Transport in Amorphous Al_2O_3 and AlF_3 for Discovery of Battery Coatings, *J. Phys. Chem. C*, 2013, **117**, 8009–8013.

10 S. C. Jung and Y. K. Han, How Do Li Atoms Pass through the Al_2O_3 Coating Layer During Lithiation in Li-Ion Batteries?, *J. Phys. Chem. Lett.*, 2013, **4**, 2681–2685.

11 Y. Wang, W. D. Richards, S. P. Ong, L. J. Miara, J. C. Kim, Y. F. Mo and G. Ceder, Design Principles for Solid-State Lithium Superionic Conductors, *Nat. Mater.*, 2015, **14**, 1026–1031.

12 L. L. Zhang, J. J. Chen, S. Cheng and H. F. Xiang, Enhanced Electrochemical Performances of $Li_{1.2}Ni_{0.2}Mn_{0.6}O_2$ Cathode Materials by Coating $LiAlO_2$ for Lithium-Ion Batteries, *Ceram. Int.*, 2016, **42**, 1870–1878.

13 J. Z. Kong, C. Ren, Y. X. Jiang, F. Zhou, C. Yu, W. P. Tang, H. Li, S. Y. Ye and J. X. Li, Li-Ion-Conductive Li_2TiO_3-Coated $Li[Li_{0.2}Mn_{0.51}Ni_{0.19}Co_{0.1}]O_2$ for High-Performance Cathode Material in Lithium-Ion Battery, *J. Solid State Electrochem.*, 2016, **20**, 1435–1443.

14 S. J. Liu, H. Wu, L. Huang, M. W. Xiang, H. Liu and Y. Zhang, Synthesis of $Li_2Si_2O_5$-Coated $LiNi_{0.6}Co_{0.2}Mn_{0.2}O_2$ Cathode Materials with Enhanced High-Voltage Electrochemical Properties for Lithium-Ion Batteries, *J. Alloys Compd.*, 2016, **674**, 447–454.

15 H. Wu, Z. Y. Wang, S. J. Liu, L. Zhang and Y. Zhang, Fabrication of Li^+-Conductive Li_2ZrO_3-Based Shell Encapsulated $LiNi_{0.5}Co_{0.2}Mn_{0.3}O_2$ Microspheres as High-Rate and Long-Life Cathode Materials for Li-Ion Batteries, *ChemElectroChem*, 2015, **2**, 1921–1928.

16 V. Singh and K. G. Rao, Studies of Defects in Combustion Synthesized Europium-Doped $LiAl_5O_8$ Red Phosphor, *J. Solid State Chem.*, 2008, **181**, 1387–1392.

17 X. G. Han, *et al.*, Negating Interfacial Impedance in Garnet-Based Solid-State Li Metal Batteries, *Nat. Mater.*, 2017, **16**, 572–579.

18 M. M. Thackeray, P. J. Johnson, L. A. Depicciotto, P. G. Bruce and J. B. Goodenough, Electrochemical Extraction of Lithium from $LiMn_2O_4$, *Mater. Res. Bull.*, 1984, **19**, 179–187.

19 C. N. Avram, M. G. Brik and A. S. Gruia, Theoretical Calculations of Energy Levels Scheme of Cr^{3+}-Doped $LiAl_5O_8$ Spinel, *Optoelectron. Adv. Mater., Rapid Commun.*, 2010, **4**, 1127–1130.

20 M. Liu, Z. Q. Rong, R. Malik, P. Canepa, A. Jain, G. Ceder and K. A. Persson, Spinel Compounds as Multivalent Battery Cathodes: A Systematic Evaluation Based on *Ab Initio* Calculations, *Energy Environ. Sci.*, 2015, **8**, 964–974.

21 M. Aykol, S. Kim, V. I. Hegde, D. Snydacker, Z. Lu, S. Q. Hao, S. Kirklin, D. Morgan and C. Wolverton, High-Throughput Computational Design of Cathode Coatings for Li-Ion Batteries, *Nat. Commun.*, 2016, 7.

22 G. Kresse and J. Furthmuller, Efficient Iterative Schemes for *Ab Initio* Total-Energy Calculations Using a Plane-Wave Basis Set, *Phys. Rev. B: Condens. Matter Mater. Phys.*, 1996, **54**, 11169–11186.

23 P. E. Blochl, Projector Augmented-Wave Method, *Phys. Rev. B: Condens. Matter Mater. Phys.*, 1994, **50**, 17953–17979.

24 J. P. Perdew, K. Burke and M. Ernzerhof, Generalized Gradient Approximation Made Simple, *Phys. Rev. Lett.*, 1996, **77**, 3865–3868.

25 D. J. Chadi, Special Points for Brillouin-Zone Integrations, *Phys. Rev. B: Solid State*, 1977, **16**, 1746–1747.

26 C. G. Van de Walle and J. Neugebauer, First-Principles Calculations for Defects and Impurities: Applications to Iii-Nitrides, *J. Appl. Phys.*, 2004, **95**, 3851–3879.

27 Y. F. Mo, S. P. Ong and G. Ceder, First Principles Study of the $Li_{10}GeP_2S_{12}$ Lithium Super Ionic Conductor Material, *Chem. Mater.*, 2012, **24**, 15–17.

28 F. D. Han, Y. Z. Zhu, X. F. He, Y. F. Mo and C. S. Wang, Electrochemical Stability of $Li_{10}GeP_2S_{12}$ and $Li_7La_3Zr_2O_{12}$ Solid Electrolytes, *Adv. Energy Mater.*, 2016, **6**, 1501590.

29 G. Mills, H. Jonsson and G. K. Schenter, Reversible Work Transition-State Theory – Application to Dissociative Adsorption of Hydrogen, *Surf. Sci.*, 1995, **324**, 305–337.

30 A. Van der Ven, G. Ceder, M. Asta and P. D. Tepesch, First-Principles Theory of Ionic Diffusion with Nondilute Carriers, *Phys. Rev. B: Condens. Matter Mater. Phys.*, 2001, **64**, 184307.

31 Y. H. Yang, Q. Wu, Y. H. Cui, Y. C. Chen, S. Q. Shi, R. Z. Wang and H. Yan, Elastic Properties, Defect Thermodynamics, Electrochemical Window, Phase Stability, and Li^+ Mobility of Li_3PS_4: Insights from First-Principles Calculations, *ACS Appl. Mater. Interfaces*, 2016, **8**, 25229–25242.

32 S. Li, J. Liu and B. Liu, First Principles Study of the Charge Transport Mechanisms in Lithium Superoxide, *Chem. Mater.*, 2017, **29**, 2202–2210.

33 R. J. D. Tilley, *Defects in Solids*, John Wiley & Sons, New York, 2008.

34 S. P. Ong, L. Wang, B. Kang and G. Ceder, Li-Fe-P-O_2 Phase Diagram from First Principles Calculations, *Chem. Mater.*, 2008, **20**, 1798–1807.

35 S. P. Ong, W. D. Richards, A. Jain, G. Hautier, M. Kocher, S. Cholia, D. Gunter, V. L. Chevrier, K. A. Persson and G. Ceder, Python Materials Genomics (Pymatgen): A Robust, Open-Source Python Library for Materials Analysis, *Comput. Mater. Sci.*, 2013, **68**, 314–319.

36 Z. Deng, Z. Y. Zhu, I. H. Chu and S. P. Ong, Data-Driven First-Principles Methods for the Study and Design of Alkali Superionic Conductors, *Chem. Mater.*, 2017, **29**, 281–288.

37 A. Jain, *et al.*, Commentary: The Materials Project: A Materials Genome Approach to Accelerating Materials Innovation, *APL Mater.*, 2013, **1**, 011002.

38 M. Kriens, G. Adiwidjaja, W. Guse, K. H. Klaska, C. Lathe and H. Saalfeld, The Crystal Structures of $LiAl_5O_8$ and $Li_2Al_4O_7$, *Neues Jb Miner. Monat.*, 1996, 344–350.

39 J. Vetter, P. Novak, M. R. Wagner, C. Veit, K. C. Moller, J. O. Besenhard, M. Winter, M. Wohlfahrt-Mehrens, C. Vogler and A. Hammouche, Ageing Mechanisms in Lithium-Ion Batteries, *J. Power Sources*, 2005, **147**, 269–281.

40 S. Q. Shi, P. Lu, Z. Y. Liu, Y. Qi, L. G. Hector, H. Li and S. J. Harris, Direct Calculation of Li-Ion Transport in the Solid Electrolyte Interphase, *J. Am. Chem. Soc.*, 2012, **134**, 15476–15487.

41 S. Q. Shi, Y. Qi, H. Li and L. G. Hector, Defect Thermodynamics and Diffusion Mechanisms in Li_2CO_3 and Implications for the Solid Electrolyte Interphase in Li-Ion Batteries, *J. Phys. Chem. C*, 2013, **117**, 8579–8593.

42 H. Yildirim, A. Kinaci, M. K. Y. Chan and J. P. Greeley, First-Principles Analysis of Defect Thermodynamics and Ion Transport in Inorganic SEI Compounds: LiF and NaF, *ACS Appl. Mater. Interfaces*, 2015, **7**, 18985–18996.

43 S. N. Li, J. B. Liu and B. X. Liu, First-Principles Study of the Charge Transport Mechanisms in Lithium Superoxide, *Chem. Mater.*, 2017, **29**, 2202–2210.

44 T. N. Chen, G. Ceder, G. S. Gautam and P. Canepa, Evaluation of Mg Compounds as Coating Materials in Mg Batteries, *Front. Chem.*, 2019, **7**, DOI: 10.3389/fchem.2019.00024.

45 Y. Z. Zhu, X. F. He and Y. F. Mo, Origin of Outstanding Stability in the Lithium Solid Electrolyte Materials: Insights from Thermodynamic Analyses Based on First-Principles Calculations, *ACS Appl. Mater. Interfaces*, 2015, **7**, 23685–23693.

46 V. Lacivita, Y. Wang, S. H. Bo and G. Ceder, *Ab Initio* Investigation of the Stability of Electrolyte/Electrode Interfaces in All-Solid-State Na Batteries, *J. Mater. Chem. A*, 2019, **7**, 8144–8155.